Thresholding complex magnetic resonance images using magnitude and Phase

Daniel B. Rowe[1-2] Ph.D. and E. Mark Haacke[3-5] Ph.D.
[1]Department of Biophysics, Medical College of Wisconsin, Milwaukee, Wisconsin, USA
[2]Division of Biostatistics, Medical College of Wisconsin, Milwaukee, Wisconsin, USA
[3]The MRI Institute for Biomedical Research, Detroit, Michigan, USA
[4]Department of Biomedical Engineering, Wayne State University, Detroit, Michigan, USA
[5]Department of Radiology, Harper University Hospital, Detroit, Michigan, USA

Abstract
It is often desirable to separate voxels that contain signal from tissue along with measurement noise from those that contain purely measurement noise. Generally this separation called thresholding utilizes only the magnitude portion of the images. Recently methods have been developed that utilize both the magnitude and phase for thresholding voxels [Pandian D, Ciulla C, and Haacke EM, Jiang J, Ayaz, M. A complex threshold method for identifying pixels that contain predominantly noise in magnetic resonance images. J Magn Reson Imaging 2008;28:727-735.]. This manuscript is an extension of that work and uses the bivariate normality of the real and imaginary values with phase coupled means. A likelihood ratio statistic is derived that simplifies to a more familiar form that is F-distributed in large samples. It is shown that in small samples, critical values from Monte Carlo simulation can be used to threshold this statistic with the proper Type I and Type II error rates. This method is applied to susceptibility weighted magnetic resonance images and shown to produce increased image contrast.

Key Words: MRI, Complex, Magnitude, Phase, Threshold, SWI

1. Introduction
In magnetic resonance images, it is well known that noise manifests as independent and identically distributed normally distributed noise in the real and imaginary parts of the k-space measurements with a mean of zero and a constant variance [1,2,3]. It is also known that there is a linear relationship between complex-valued k-space measurement and complex-valued voxel measurements [4]. From the normality of k-space measurements and their linear relationship with voxel measurements, the voxel measurements are also normally distributed [1,2,4]. Voxel measurements can be described as

$$y_R = \rho\cos\theta + \varepsilon_R, \qquad y_I = \rho\sin\theta + \varepsilon_I \tag{1}$$

where y_R and y_I are the measurements for the real and imaginary parts, ε_R and ε_I are the error terms for the real and imaginary parts, while ρ and θ are the population magnitude and phase. It is desirable to separate voxels that are pure noise from those that contain signal and noise [5]. Assuming that the additive noise terms in Eq. (1) are normally distributed with a mean of zero and variance σ^2, the joint probability distribution of the bivariate voxel observation (y_R,y_I) is

$$p(y_R, y_I \mid \rho,\theta,\sigma^2) = \frac{1}{\sqrt{2\pi\sigma^2}}\exp\left[-\frac{(y_R-\rho\cos\theta)}{2\sigma^2}\right]\cdot\frac{1}{\sqrt{2\pi\sigma^2}}\exp\left[-\frac{(y_I-\rho\sin\theta)}{2\sigma^2}\right]. \tag{2}$$

Upon conversion from Cartesian coordinates to polar coordinates in Eq. (2), the joint distribution of the observed magnitude and phase (m,φ) is

$$p(m,\phi \mid \rho,\theta,\sigma^2) = \frac{m}{2\pi\sigma^2}\exp\left\{-\frac{1}{2\sigma^2}\left[m^2+\rho^2-2\rho m\cos(\phi-\theta)\right]\right\}. \tag{3}$$

We would like to determine if the observed magnitude and phase in a voxel are signal or if they are noise. Given a collection of measurements $(m_1,\varphi_1),\ldots,(m_n,\varphi_n)$ from $p(m,\varphi)$ in Eq. (3), the likelihood is

$$L(\rho,\theta,\sigma^2) = \left(2\pi\sigma^2\right)^{-n}\left[\prod_{i=1}^{n} m_i\right]\exp\left\{-\frac{1}{2\sigma^2}\sum_{i=1}^{n}\left[m_i^2+\rho^2-2\rho m_i\cos(\phi_i-\theta)\right]\right\}. \tag{4}$$

It is desirable to increase image contrast by thresholding noise voxels where the magnitude and phase are not statistically different from zero from those where the magnitude and phase are statistically different from zero. This separation of voxels that contain signal (within the object being imaged) has been described by other means that use an

estimate of the variance from voxels that contain pure noise [5]. We will show in the next section that a formal statistic can be derived from Eq. (4) and a statistical hypothesis test performed on the population magnitude and phase.

2. Methods

In statistics the formal procedure to separate voxels that contain noise from those that also contain signal is to perform a hypothesis test on the magnitude and phase. In hypothesis testing there are four possible outcomes that are depicted in Table 1. In the top right and bottom left cells correct decisions are made. In the top left shaded cell a Type I error is made in which the null hypothesis is rejected when it is true. The probability of a Type I error is the level of significance denoted by α. In the bottom right shaded cell a Type II error is made in which the null hypothesis is not rejected when it is false. The probability of a Type II error is the level of significance denoted by β. These two error rates will be examined in more detail later.

Table 1. Four outcomes from a hypothesis test.

	H_0 True	H_0 False
Reject H_0	Type I Error (α)	Correct Decision (1- α)
Do Not Reject H_0	Correct Decision (1-β)	Type II Error (β)

Formally, this voxel separation procedure can be achieved by testing null and alternative hypotheses H_0: $\rho=0$, $\theta=0$ versus H_1: $\rho>0$, $\theta\neq 0$ where ρ is the population magnitude and θ is the population phase. In general, hypotheses can be evaluated with test statistics that are derived via a likelihood ratio statistic [6,7]. Under the constrained null hypothesis H_0: $\rho=0$, $\theta=0$, the maximum likelihood estimators (MLEs) for the magnitude and phase are

$$\tilde{\rho}=0,\tilde{\theta}=0,\quad \tilde{\sigma}^2=\frac{1}{2n}\sum_{i=1}^{n}\left(y_{Ri}^2+y_{Ii}^2\right) \tag{5}$$

while under the unconstrained alternative hypothesis H_1: $\rho>0,\theta\neq 0$ they are

$$\hat{\rho}=\left[\left(\bar{y}_R\right)^2+\left(\bar{y}_I\right)^2\right]^{\frac{1}{2}},\quad \hat{\theta}=\tan^{-1}\left[\sum_{i=1}^{n}y_{Ii}\Big/\sum_{i=1}^{n}y_{Ri}\right],\quad \hat{\sigma}^2=\frac{1}{2}\sum_{i=1}^{n}\left(y_{Ri}^2+y_{Ii}^2\right)-\frac{1}{2}\left[\left(\bar{y}_R\right)^2+\left(\bar{y}_I\right)^2\right] \tag{6}$$

where $\bar{y}_R$ is the mean of the real channel measurements and $\bar{y}_I$ is the mean of the imaginary channel measurements. These estimates in Eq. (5) and Eq. (6) are then inserted back into the likelihoods and the ratio $\lambda=L(\tilde{\rho},\tilde{\theta},\tilde{\sigma}^2)\big/L(\hat{\rho},\hat{\theta},\hat{\sigma}^2)$ taken. Under some regularity conditions (that are satisfied in this case), -2log(λ) is asymptotically χ^2 distributed with degrees of freedom equal to the difference in the number of estimated parameters between H_0 and H_1, (two in this case). However, algebra can usually be performed (as described in the Appendix) to simplify this into a statistic with known distribution under the null hypothesis. This procedure can be applied to the general linear model to derive the usual t and F statistics. Applying this procedure here, the test statistic

$$F=\left(\frac{n\left[\left(\bar{y}_R\right)^2+\left(\bar{y}_I\right)^2\right]\Big/\sigma^2}{2}\right)\Big/\left(\frac{\left[\sum_{i=1}^{n}y_{Ri}^2+\sum_{i=1}^{n}y_{Ii}^2\right]\Big/\sigma^2}{2n}\right) \tag{7}$$

can be arrived at (as described in the Appendix). Further, one can show (as in the Appendix) that

$$x_1=n\left[\left(\bar{y}_R\right)^2+\left(\bar{y}_I\right)^2\right]\Big/\sigma^2 \tag{8}$$

is χ^2 distributed with two degrees of freedom and that

$$x_2=\left[\sum_{i=1}^{n}y_{Ri}^2+\sum_{i=1}^{n}y_{Ii}^2\right]\Big/\sigma^2 \tag{9}$$

is χ^2 distributed with $2n$ degrees of freedom. The test statistic in Eq. (7) denoted by F is found by dividing these by their degrees of freedom and taking ratio.

This statistic denoted by F should have an F distribution with two numerator and $2n$ denominator degrees of freedom when the null hypothesis is true. However, that is only if the two χ^2 statistics x_1 and x_2 in the numerator and

denominator are statistically independent. It can be shown (as in the Appendix) that their correlation is $1/\sqrt{n}$. The test statistic F has an asymptotic large sample F distribution with two numerator and $2n$ denominator degrees of freedom for large n. In non-fMRI applications where there may be a very small number of repeated images if any, this asymptotic result does not hold. Thus, critical values from the F distribution do not apply to this F statistic. However, critical values for small n can be achieved via Monte Carlo simulation. For a given level of significance (Type I error rate α), we reject H_0 (do not threshold voxel) if the test statistic F is larger than the critical value $F_\alpha(2,2n)$ and do not reject (threshold voxel) if F is smaller.

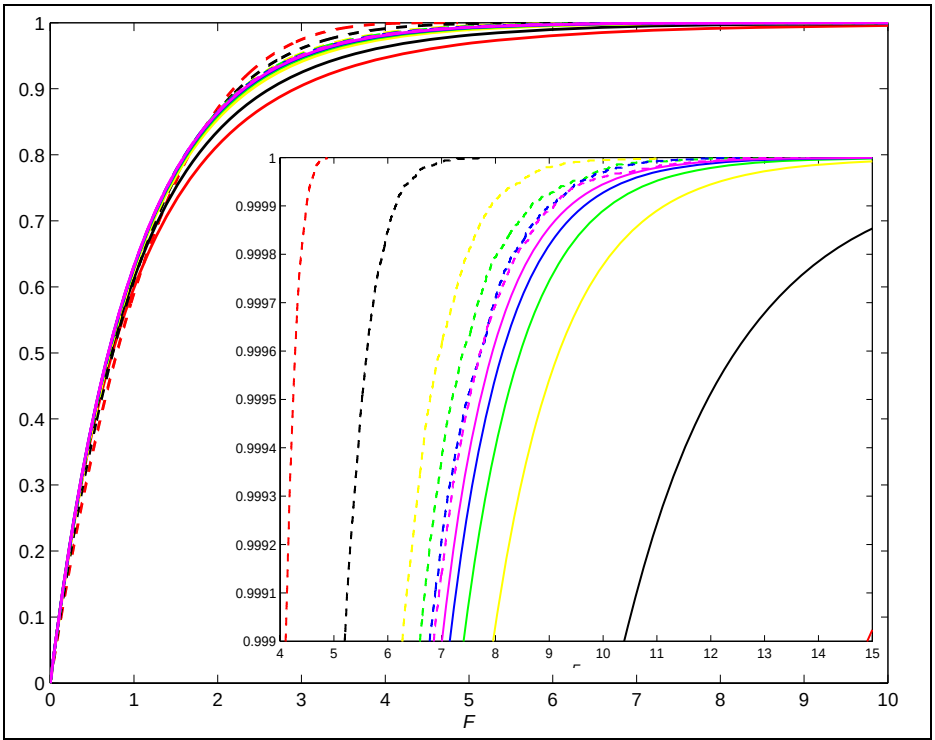

Figure 1: CDF from Monte Carlo simulation (dashed) and F distribution (solid) for $n=5$ (red), 9 (orange), 25 (yellow), 50 (green), 100 (blue), 250 (violet).

To examine the convergence of the distribution of the F statistic to the F distribution, one million simulated data sets was created under the null hypothesis ($\rho=0$ and $\theta=0$) for $n=5, 9, 25, 50, 100,$ and 250. Normally distributed independent noise variates were generated for the real and imaginary parts with a variance of $\sigma^2=1$. This corresponds to a signal-to-noise ratio (SNR) of zero. It was found (but not shown), that regardless of the sample size n, the two statistics x_1 and x_2 in Eq. (8) and Eq. (9) that make up the numerator and denominator are χ^2 distributed. Additionally, the $1/\sqrt{n}$ correlation between the numerator and denominator χ^2 statistics was verified. For each sample size n, the F statistic was computed for each of the data sets. Cumulative distribution functions (CDFs) from the Monte Carlo empirical distributions (dashed curves) and corresponding CDF for the F distribution (solid curves) are presented in Figure 1 for $n=5$ (red), 9 (orange), 25 (yellow), 50 (green), 100 (blue), 250 (violet). Note the disparity between the Monte Carlo empirical distributions (dashed curves) and corresponding CDF for the F distribution (solid curves). One can see that it takes a relatively large sample size for this disparity to decrease. Therefore for small samples, Monte Carlo critical values need to be used.

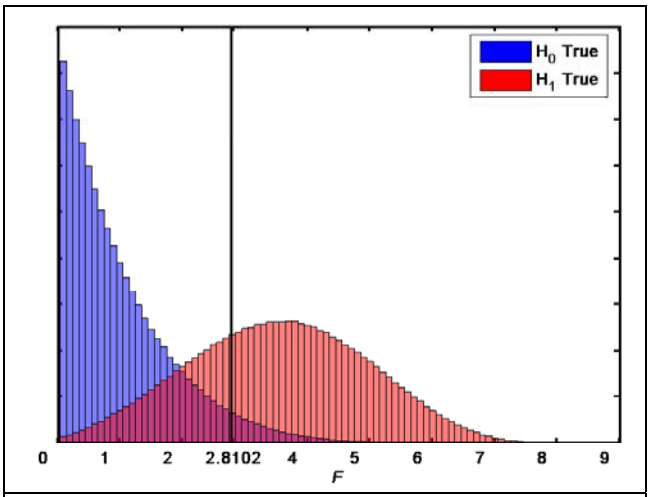

Figure 2: Histogram when H_0 is true and when and when H_1 is true.

For our application, we will be utilizing the test statistic denoted by F for a sample of size $n=9$. The Type I error rate was examined in Figure 1 for several values of n. However, the Type II rate is also of interest. To examine the Type II error rate, one million simulated data sets for $n=9$ were created under the alternative hypothesis ($\rho\neq0$ and $\theta\neq0$) with $\rho=(0,1,2,3,5)$ and $\theta=0°$. Normally distributed independent noise variates were generated for the real and imaginary parts with a mean of zero and a variance of $\sigma^2=1$. Figure 2 shows histograms for the million data sets when $\rho=0$ in blue and $\rho=1$ in red. The vertical line is at $F_{.05}=2.8102$ which is the critical value with $\alpha=0.05$. The false positive rate α is the magenta colored area that is to the right of F_α. The blue and magenta colored areas less than F_α are

the true positive rate *1-α*. The red and magenta areas to the right of F_α are the true negative rate *1-β*. The false negative rate *β* is the magenta and red colored areas that are to the left of F_α. By sliding this vertical line left and right for varying false positive rate areas *α* to the right of it, we can determine the true positive rate *1-β*. A plot of *α* on the horizontal axis and *1-β* on the vertical axis is called a receiver operating characteristic (ROC) curve [8]. This curve can be made for each combination of *ρ* and *θ*. In Figure 3 are the ROC curves for *ρ=(0,1,2,3,5)* and *θ=0°*. When *θ≠0*, minor variations from the curves for the corresponding *ρ* value are produced.

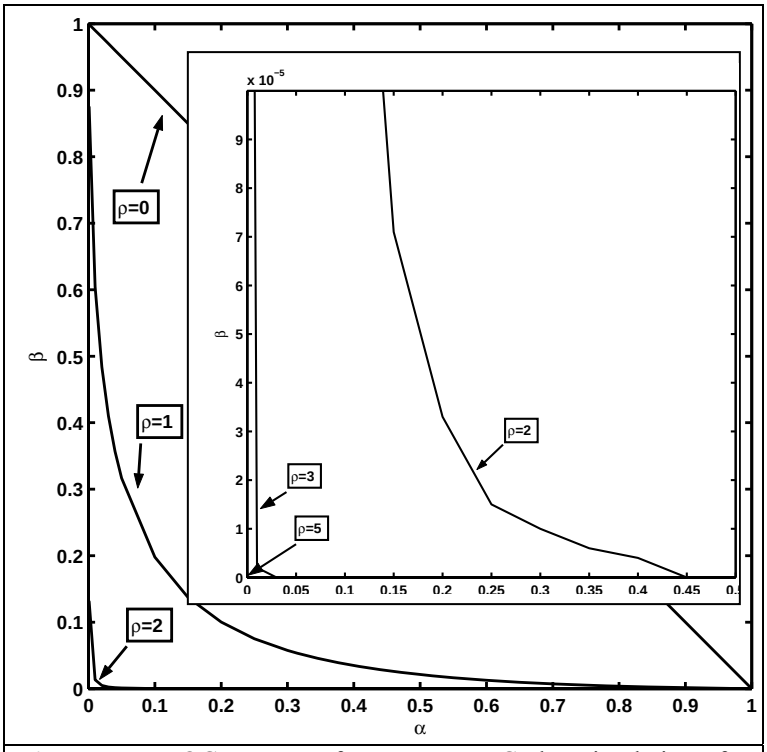

Figure 3: ROC curves from Monte Carlo simulation for *ρ=(0,1,2,3,5)* and *θ=0°*.

To determine more accurate critical values in the upper tail of the *F* statistic for *n=9*, 5×10^7 data sets were generated. For each set, the F statistic was computed. A histogram of these *F* statistics for *n=9* is presented in Figure 4. These *F* statistics were ordered and percentiles determined. For example, the $0.95\times(5\times10^7)^{th}$ largest value was taken as the 95^{th} percentile. Selected critical values are presented in Table 2 for *n=5* and *n=9*. These critical values will be used for thresholding the magnitude and phase of voxels. Additional critical values can reliably be interpolated.

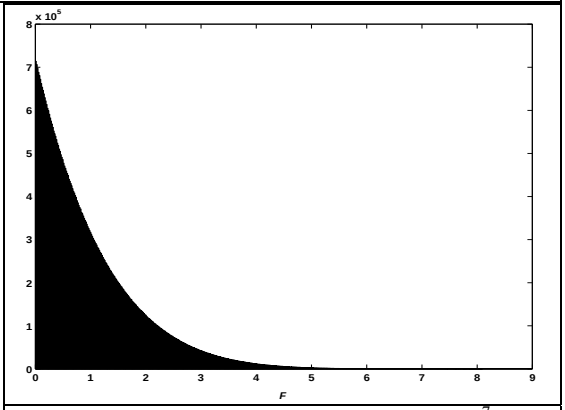

Figure 4: Histogram of *F* statistic for 5×10^7 data sets under null hypothesis for critical values.

From a statistical point of view, we would like to have *n* repeated images. However, we are interested in thresholding high-resolution anatomical images where replicated images are rarely available. We will use the observed magnitude and phase values in each voxel and its surrounding voxels. Each voxel and its eight neighbors (*n*=9) will be used to estimate the magnitude and phase of every voxel with image wrap around. Alternative each voxel and its four neighbors (*n*=5) can be used. The estimated values for each voxel will be used to compute the described *F* statistic. The map of these *F* statistics is thresholded with the critical values in Table 2. A zero-one mask is produced from the thresholded *F* statistics then applied to the original magnitude and phase images.

Table 2. Critical *F* statistic values for *n=5* and *n=9*.

n=5									
α	.05	.01	.001	.001	.0001	.000001	.05/256/256	.05/512/352	.05/512/512
F_α	2.6355	3.4189	4.1104	4.4992	4.7162	4.8445	4.8617	4.8776	4.8874
n=9									
α	.05	.01	.001	.0001	.00001	.000001	.05/256/256	.05/512/352	.05/512/512
F_α	2.8102	3.9377	5.1991	6.1512	6.8678	7.3911	7.5627	7.5869	7.7575

Since only a single image is available, using a voxel and its neighboring voxel will result in minor local correlation in the *F* statistics. A statistical critical value for a given *α* level might be slightly lower than the values we have used from the Monte Carlo simulation. To investigate this phenomenon, additional simulations were performed where images were created and the *F* statistics computed using a voxel and its four neighbors. Images of size 352×512 and 1000×1000 were created where each voxel had a magnitude of *ρ=(0,1,2,3,5)* and a phase of *θ=0°*. Normally distributed independent noise variates were generated and added to the real and imaginary parts with a mean of zero and a variance

of σ^2=1. ROC curves were produced for each magnitude (equivalently SNR) value. The fraction of true positives and false positives were determined. The false positive α and false negative rates β were consistent with previous values and yielded visually identical ROC curves as seen in Figure 3. Simulations were also performed in which 512×512 images were produced with a circle of radius 128 pixels containing the same magnitudes of ρ=(*0,1,2,3,5*) and a phase of θ=*0*°. True and false positive rates were also consistent as were ROC curves. The small local correlation does not affect the global image threshold as previous reports suggest [9].

3. Results

Susceptibility weighted imaging (SWI) [10] MRI data is used to test the noise removal procedure both in magnitude and phase. A SWI brain volume was acquired on a 3T Siemens Trio with a matrix size of 352×512, FOV of 176 mm × 256 mm, and an in-plane resolution of 0.5×0.5 mm^2, TR=26 ms, TE= 15 ms, flip angle (FA) = 11^o [8].

The magnitude and phase statistical thresholding method described in this paper was applied to the human leg SWI data. The results from this analysis are presented in Figs. 5, 6, and 7. In Figure 5A and Figure 5B the original observed SWI magnitude and phase image data are respectively presented. Note that in Figure 5B there is high noise in the phase image outside the body and in some internal areas while the magnitude noise in Figure 5A is relatively low. The magnitude and phase model was applied to each voxel using its eight neighbors for samples of n=*9*. In Figure 5C and Figure 5D the estimated SWI magnitude and phase image data are respectively presented. Note that there is a reduction in the high frequency image content. In Figure 5E the estimated voxel variance is presented. Note that some high frequency spatial content is present in Figure 5E. In Figure 5F the F statistic map that is used for thresholding is presented. Note that spatial anatomical structure is present in Figure 5F where voxels with larger magnitude and phase have larger F statistics.

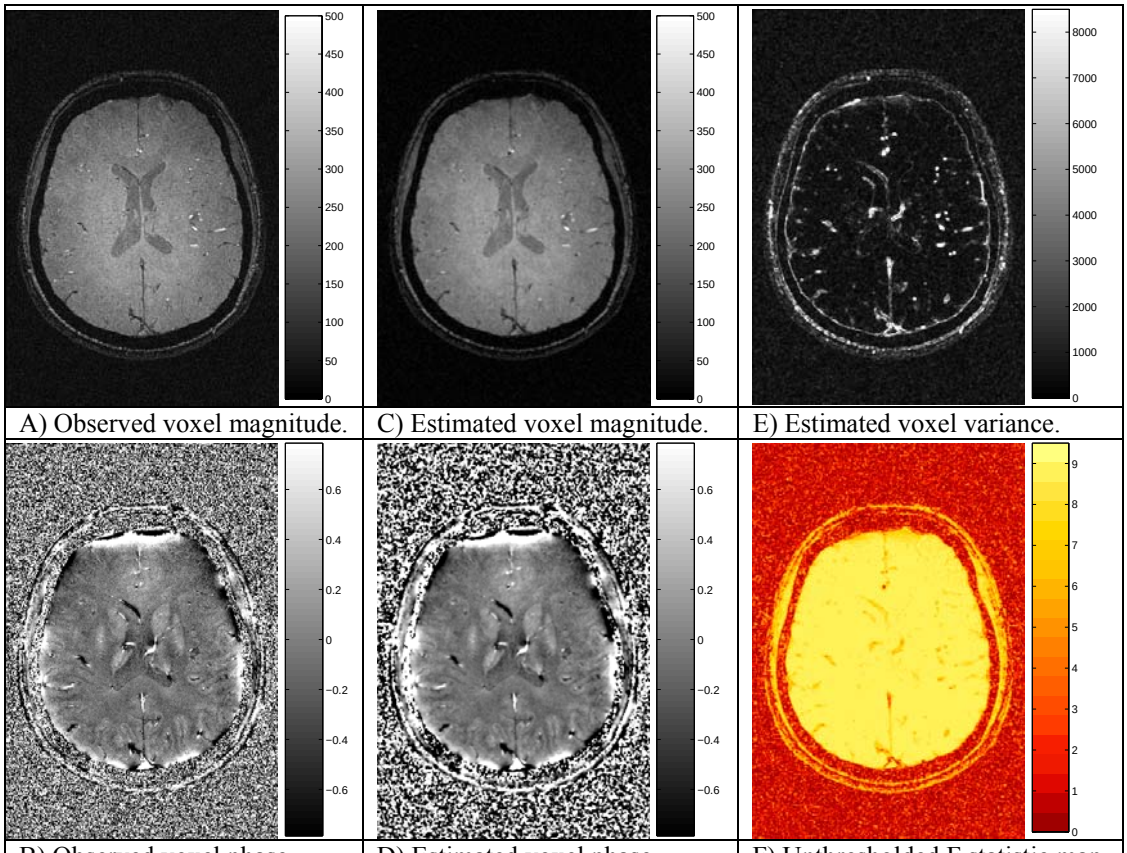

Figure 5: Observed and estimated image values.

In Figure 6A and Figure 6B histograms of the original observed SWI magnitude and phase image data are respectively presented. Note that in Figure 6A, the observed magnitude contains two populations of voxels that visually are fairly easily distinguishable. The first population has high magnitude (SNR) values while the second has low magnitude

(SNR) values. In Figure 6B, the observed phase contains two populations of voxels that are much more difficult to visually distinguish. The first population of voxels has phase values that are distributed closely around zero. The second population of voxels has phase values that a more uniformly distributed in the $-\pi$ to π interval. The marginal distribution of the phase is uniform when $\rho=0$. In Figure 6C the two populations of voxels are still visually present but appear to have greater separation. In Figure 6D, there appears to be slightly fewer voxels with phase values near $\pm\pi$ and more near zero. In Figure 6E, it can be seen that most voxels have a small estimated variance but there are some with very large variances that span the entire horizontal axis. In Figure 6F, it is obvious that there are F statistic values from two different distributions. The first distribution is for large values of the F statistic (corresponding to large magnitude and or phase voxels) that tapers for smaller F statistic values. The second distribution is on the smaller side for smaller F statistic values (corresponding to small magnitude and or phase voxels) that tapers for larger F statistic values. Note the similarity between this second distribution for small F statistic values and the distribution of F statistic values in Figure 4 when no magnitude or phase signal is present (i.e. the null hypothesis is true).

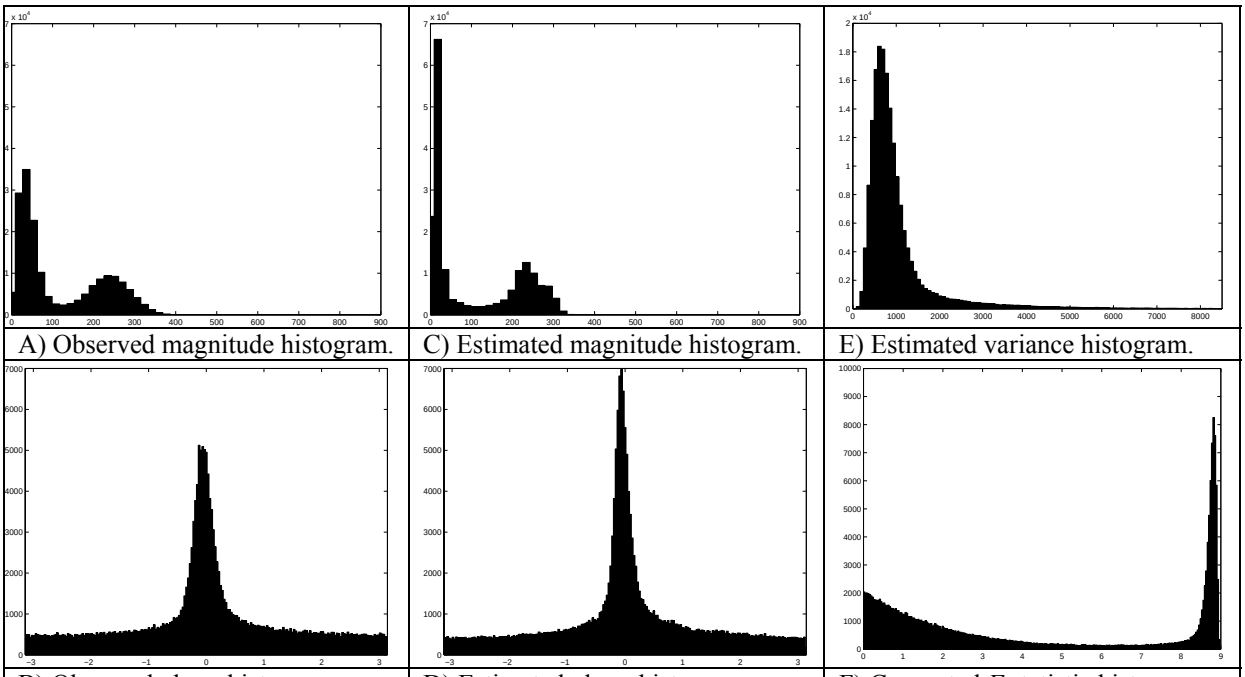

A) Observed magnitude histogram. | C) Estimated magnitude histogram. | E) Estimated variance histogram.

B) Observed phase histogram. | D) Estimated phase histogram. | F) Computed F statistic histogram.

Figure 6: Histograms of observed and estimated image values.

The map of these F statistics in Figure 5F is thresholded with the critical values in Table 2 for α = 0.05, 0.0001, and 0.05/512/352. A zero-one mask is produced from the thresholded F statistics then applied to the original magnitude and phase images in Figure 5A and Figure 5B respectively. Thresholded original observed images are presented in Figs. 7. The magnitude and phase of thresholded voxels are set to zero but for display the thresholded phase voxel values are set to $-\pi$. In Figure 7A and Figure 7B the images are thresholded at F=2.8102, in Figure 7C and Figure 7D the images are thresholded at F=6.1512, in Figure 7C and Figure 7D the images are thresholded at F=7.5869. A vertical line can be drawn in Figure 4 (that contains the distribution of F statistics under the null hypothesis) and in Figure 6F (that contains the observed F statistics with both null and alternative hypothesis statistics) for each of these threshold values. Note in Figure 7 that as the false positive rate decreases from Figure 7A and Fig 7B to Figure 7E and Figure 7F, the number of voxels outside of the head decreases but more voxels within the head are also eliminated. This phenomenon is due to the relationship between Type I and Type II error rates as illustrated in Figure 2. It is apparent that the magnitude image in Figure 7E shows similar anatomical to the phase image in Figure 7F indicating similar biological information.

4. Discussion and Conclusions

A recent approach to suppress noise also used a complex threshold method (CTM) [5]. This method used not only complex thresholding but also connectivity to enhance suppression of noise or prevent the incorrect assignment of signal to noise to reduce Type I errors. We do not use connectivity in this approach since we are looking at local variance on a pixel by pixel basis. Also, the CTM [5] suffers when the phase itself deviates from zero or any set zero

point. This can lead to the suppression of areas where the phase is offset from flow effects or susceptibility effects (the later being acceptable in some cases when the goal is to also suppress veins). However, the phase has a rapid variation near air/tissue interfaces, particularly at the front of the head in Figure 5B for example. In that area the CTM method [5] would fail and that part of the brain will be suppressed. Not so with this approach where we look specifically at the local variance and keep the local value as the phase offset (i.e., there is not a global offset of zero in phase). For this reason, this new approach is more robust to variations in phase caused by unwanted field inhomogeneity effects.

In summary, a magnitude and phase statistical thresholding procedure based upon a likelihood ratio test was presented. It was shown through Monte Carlo simulation that this method operates according to its theoretical statistical properties in terms of both false positives and false negatives. This statistical thresholding method was successfully applied to real human SWI data and shown to produce increased image contrast by eliminating false positives.

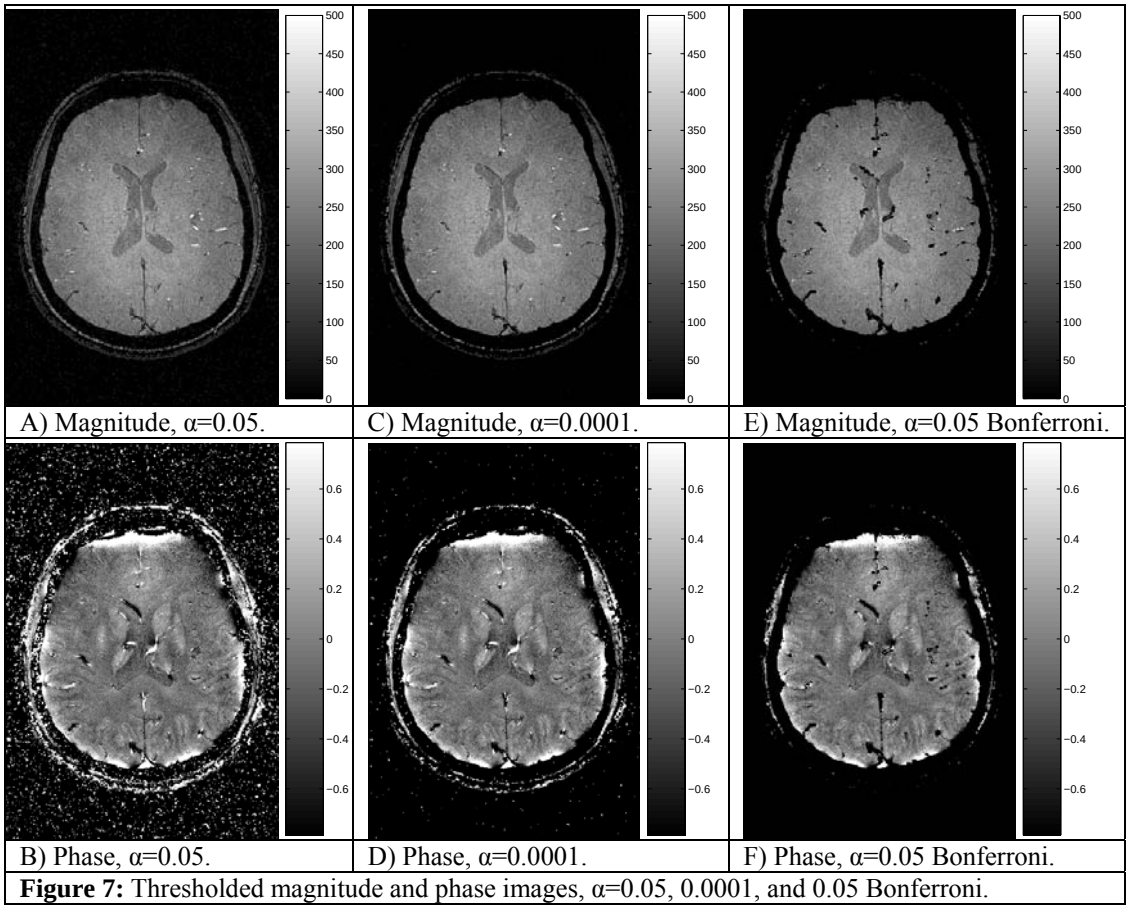

Figure 7: Thresholded magnitude and phase images, α=0.05, 0.0001, and 0.05 Bonferroni.

5. Appendix

In deriving the *F* statistic, first maximum likelihood estimators are found first assuming the null hypothesis H_0 is true then assuming the alternative hypothesis H_1 is true. These estimators are inserted into the likelihood function and the ratio taken Algebra is performed and this ratio simplified into a more familiar form.

When it is assumed that the null hypothesis H_0: $\rho=0$, $\theta=0$ is true, the likelihood in Eq. (4) is maximized. From the null hypothesis constraints, the MLEs for ρ and θ are that they are zero as given in Eq. (5). By differentiating the log likelihood with respect to the variance σ^2 then setting this result equal to zero and solving, its MLE can be found as in Eq. (5). When it is assumed that the alternative hypothesis H_1: $\rho>0$, $\theta\neq0$ is true, the likelihood in Eq. (4) is maximized. By differentiating the log likelihood with respect to the magnitude ρ, the phase θ, and variance σ^2 then setting this result equal to zero and solving, the parameter MLEs can be found as in Eq. (6).

These MLEs are inserted back into the likelihood function and the ratio of null hypothesis likelihood over alternative hypothesis $\lambda = L(\tilde{\rho},\tilde{\theta},\tilde{\sigma}^2)/L(\hat{\rho},\hat{\theta},\hat{\sigma}^2)$ taken. Upon insertion and cancellation of some terms, the likelihood ratio is

$$\lambda = \frac{\left[\frac{1}{2n}\sum_{i=1}^{n} m_i\right]^{-n}}{\left[\frac{1}{2n}\sum_{i=1}^{n} m_i - \frac{1}{2}\hat{\rho}^2\right]^{-n}}, \quad \lambda^{\frac{1}{n}} = \frac{\left[\frac{1}{2n}\sum_{i=1}^{n}\left(y_{Ri}^2 + y_{Ii}^2\right) - \frac{1}{2}\left[\left(\bar{y}_R\right)^2 + \left(\bar{y}_I\right)^2\right]\right]}{\left[\frac{1}{2n}\sum_{i=1}^{n}\left(y_{Ri}^2 + y_{Ii}^2\right)\right]} \tag{A.1}$$

From Eq. (A.1), some algebraic simplification leads to $F = (1-\lambda^{1/n})$ and yields Eq. (7). The probability distribution of this statistic needs to be found. The steps through the logic for the derivation of the distribution for the numerator and the denominator of the *F* statistic are shown below in Table 3.

Since the numerator and denominator terms x_1 and x_2 are χ^2 distributed with 2 and 2n degrees of freedom, dividing them by their degrees of freedom and taking the ratio should result in a statistic that under the null hypothesis has an F distribution with 2 and 2n degrees of freedom. However, this is not true in this case. These two χ^2 statistics must be statistically independent for this to be true. The correlation between these two statistics can be derived. First, since these are χ^2 distributed, their expectation is their degrees of freedom and their variances are twice their degrees of freedom $E(x_1)=2$, $E(x_2)=2n$, $var(x_1)=4$, $var(x_2)=4n$. The covariance can be found as $cov(x_1,x_2)=E(x_1x_2)-E(x_1)E(x_2)$ where it can be shown that $E(x_1x_2)=4n+4$. The correlation between x_1 and x_2 is now $1/\sqrt{n}$. This correlation tends to zero in large samples and the *F* statistic becomes F distributed.

Table 3. Derivation of the distribution of the chi square statistics. Numerator term (left) denominator term (right)

y_{Ri}	$\sim N(0,\sigma^2)$	y_{Ri}	$\sim N(0,\sigma^2)$
y_{Ri}/σ	$\sim N(0,1)$	y_{Ri}/σ	$\sim N(0,1)$
$\sum_{i=1}^{n} y_{Ri}/\sigma$	$\sim N(0,n)$	$\left(y_{Ri}/\sigma\right)^2$	$\sim \chi^2(1)$
$\sqrt{n}\,\bar{y}_R/\sigma$	$\sim N(0,1)$	$\sum_{i=1}^{n}\left(y_{Ri}/\sigma\right)^2$	$\sim \chi^2(n)$
$n\left(\bar{y}_R/\sigma\right)^2$	$\sim \chi^2(1)$	$x_2 = \frac{1}{\sigma^2}\left[\sum_{i=1}^{n} {y_{Ri}}^2 + \sum_{i=1}^{n} {y_{Ii}}^2\right]$	$\sim \chi^2(2n)$
$x_1 = \frac{n}{\sigma^2}\left[\left(\bar{y}_R\right)^2 + \left(\bar{y}_I\right)^2\right]$	$\sim \chi^2(2)$		

References

[1] Henkelman RM. Measurement of signal intensities in the presence of noise in MR images. Med Phys 1985;12:232-233.

[2] Bernstein MA, Thomasson DM, Perman WH. Improved detectability in low signal-to-noise ratio magnetic resonance images by means of phase corrected real reconstruction, Med Phys 1989;16:813-817.

[3] Macovski A. Noise in MRI. Magn Reson Imaging 1996;38:494-497.

[4] Rowe DB, Nencka AS, Hoffmann RG. Signal and noise of Fourier reconstructed fMRI data. J Neurosci Methods 2007;159:361-369.

[5] Pandian D, Ciulla C, and Haacke EM, Jiang J, Ayaz, M. A complex threshold method for identifying pixels that contain predominantly noise in magnetic resonance images. J Magn Reson Imaging 2008;28:727-735.

[6] Hogg RV and Craig AT. Introduction to Mathematical Statistics. Fourth Edition. Macmillan Publishing Company. NY, NY 1978.

[7] Bain LM and Engelhardt M. Introduction to Probability and Mathematical Statistics. Second Edition. PSW-Kent Publishing Company. Boston, MA. 1992.

[8] Haacke EM, Brown RW, Thompson MR, Venkatesan R. MRI: Physical principles and sequence design, John Wiley and Sons 1999.

[9] Logan BR and Rowe DB. An evaluation of thresholding techniques in fMRI analysis. Neuroimage 2004;22:95-108.

[10] Haacke EM, Xu Y, Cheng YCN, Reichenbach J. Susceptibility weighted imaging (SWI). Magn Reson Med 2004;52:612-618.